Measurement Science and Technology

100 year anniversary
Measurement Science and Technology

PURPOSE-LED PUBLISHING™

PAPER

Efficient machine learning method for spatio-temporal water surface waves reconstruction from polarimetric images

To cite this article: Noam Ginio *et al* 2023 *Meas. Sci. Technol.* **34** 055801

View the article online for updates and enhancements.

You may also like

- The generalized Giambelli formula and polynomial KP and CKP tau-functions
Victor Kac and Johan van de Leur
- Water wave measurement from stereo images of specular reflections
Daniel Kiefhaber, Guillemette Caulliez, Christopher J Zappa et al.
- Adaptive polarimetric image representation for contrast optimization of a polarized beacon through fog
Swapnesh Panigrahi, Julien Fade and Mehdi Alouini

This content was downloaded from IP address 132.69.243.173 on 23/12/2024 at 07:55

IOP Publishing Measurement Science and Technology
Meas. Sci. Technol. **34** (2023) 055801 (11pp) https://doi.org/10.1088/1361-6501/acb3eb

Efficient machine learning method for spatio-temporal water surface waves reconstruction from polarimetric images

Noam Ginio[1], Dan Liberzon[1,3,*], Michael Lindenbaum[2,3] and Barak Fishbain[1]

[1] Faculty of Civil and Environmental Engineering, Technion, Haifa, Israel
[2] Faculty of Computer Science, Technion, Haifa, Israel
[3] Interdisciplinary program for Ocean Engineering, Technion, Haifa, Israel

E-mail: liberzon@technion.ac.il

Received 5 October 2022, revised 2 January 2023
Accepted for publication 17 January 2023
Published 6 February 2023

Abstract

Accurate and cost-effective sea state measurements, in terms of spatio-temporal distribution of water surface elevation (water waves), is of great interest for scientific research and various engineering, industrial, and recreational applications. To this end, numerous measurement techniques have been developed over the years. None of these techniques, however, are universally applicable across various ocean and laboratory conditions and none provide near-real-time data. We utilized the latest advances in polarimetric imaging to develop a new remote sensing method based on machine learning methodology and polarimetric reflection measurements for inferring surface waves elevation and slope. The method utilizes a newly available, inexpensive polarimetric camera providing images of the water surface in a high spatio-temporal resolution at several linear polarization angles. Algorithms based on artificial neural networks (ANNs) are then trained to obtain high-resolution reconstructions of the water surface slope state from those images. The ANNs are trained on laboratory-collected supervised datasets of prescribed mechanically generated monochromatic wave trains and tested on a stochastic wave field of JONSWAP spectral shape. The proposed method, based on inferring the surface slope from polarimetric images, provides a dense estimate of the water surface. The results of this study pave the way for the development of accurate and cost-effective near-real-time remote sensing tools for both laboratory and open sea wave measurements.

Keywords: water waves, instantaneous water surface elevation and slope, polarimetric imaging, machine learning, artificial neural networks (*ANN*s), spatio-temporal near-real-time reconstruction, energy density and directional spectra

1. Introduction

Water surface waves propagate across large distances, transfer energy, induce water motion and sediment transport, and interact with shores and marine structures. Hence, understanding water waves phenomena is essential for engineering, environmental sciences, and safety applications. Most water wave fields are excited by wind, and propagate and evolve in time and space under the wind forcing. Research of this complex and stochastic phenomenon requires the capacity to produce measurements of wave fields across a large range of spatial dimensions, wave heights, and propagation speeds [1].

To produce a directional wave field energy density spectrum and enable accurate, near-real-time monitoring and

* Author to whom any correspondence should be addressed.

 © 2023 IOP Publishing Ltd

short-time projections of waves' motion and induced forces, a high spatio-temporal resolution sensing method is required. To this end, wave gauge probes (WGs) have been used broadly in laboratory setups to obtain instantaneous water surface elevation fluctuations measurements. Such probes provide a reliable temporal point measurement of the water surface elevation fluctuations. When several WGs are deployed in a spatial array, with additional processing, one can obtain spatio-temporal water surface elevation data [2–4]. However, WGs' inherent shortcoming is that they produce point measurement only; and thus, obtaining dense spatial information requires sophisticated processing techniques, which are computationally heavy to undertake and are limited in accuracy. Further, these methods are sensitive to mechanical damage and electrical interference.

Acoustic techniques include pressure sensors and acoustic Doppler current profilers. These techniques have limited frequency response and produce only low temporal resolution point measurements of waves [3]. Radar techniques are used for mapping the sea state from shores, ships, or even planes and satellites, enabling sea state assessment over large areas. However, radar techniques are expensive to implement and generally suffer from low spatial resolution [5]. Available photometric techniques include light detection and ranging sensors and visible-light stereo imaging. The use of these techniques for waves mapping requires complex calibrations and costly data processing [6]. Moreover, the main inherent complexity of stereo imaging arises from the need to find corresponding features in images that consist of similar periodic patterns, such as water waves [5, 7].

Most of the above shortcomings can be effectively addressed by a polarimetric approach, introduced by Zappa *et al* [8], using a single camera equipped with linear polarization filters. The basic principal of this approach is that unpolarized light, when reflected from the water surface, is polarized with high correlation to the local wave's slope. To deduce the functional relationship between local slope and the reflected light polarization, Zappa *et al* proposed a simplified physical model leading to closed-form analytical expressions of the slope. The simplifying assumptions include inter alia, high water turbidity, and purely unpolarized skylight conditions. The former assumption suits some coastal areas, shallow lakes, and rivers, while in deep water the turbidity is generally very low. Sun light, unpolarized at its source, reaches the earth surface by passing through the atmosphere. On its way, it is scattered by air molecules, suspended particles, and aerosols. The scattering particles are small compared to the light wavelengths and therefore the scattering follows the Rayleigh scattering principle. The positioning of the scattering elements is random, making the scattering from the various elements incoherent. As a result, the skylight reaching the water's surface is partially polarized, a combination of the unpolarized sun light with the addition of a linearly polarized component [9]. Therefore, assuming purely unpolarized light also does not hold in a wide range of natural conditions. Hence, in a variety of general conditions, the solution cannot be achieved analytically as the full system of equations describing the polarization-to-slope transfer is over-defined. Moreover, it is important to note that Zappa *et al* [8] demonstrated measurement of only the shortest waves in the spectrum, with wavelengths in the order of 10 cm.

Several laboratory and open sea studies have shown the effectiveness of the polarimetric approach [8, 10–12]. However, the physical models have been shown to be of low accuracy and their use in various open sea and lighting conditions has been shown to be limited. Furthermore, due to technical limitations and the discontinuity of the water level slope during waves breaking, the nature of collected polarimetric data in a complex wave field is expected to be incomplete or imprecise. This poses an additional difficulty for the physical model solutions, and the challenge to resolve the full spectrum of wave lengths still stands. To cope with these issues, we describe here a machine learning (ML) methodology to infer the polarization-to-slope transfer in generalized conditions that fully resolves the surface waves spectrum.

The use of ML methodologies for sea waves analysis is not new, and the approach shows good applicative potential. Cannata *et al* [13] reported the use of statistical analysis and ML random forest methodology to infer the wave heights from ubiquitous seismic noise, generated by energy transfer from the ocean to the solid earth. Shao *et al* [14] demonstrated wave data retrieval by recorded synthetic aperture radar images. The core of their methodology was a numeric wave model, which simulated a wave field, to which recorded waves were compared through random forest and decision tree ML methodologies. In a similar fashion, James *et al* [15] used ML regression and classification methodologies to infer the formation of sea waves generated by a physical model. These three studies presented capabilities for obtaining measurements of larger wave lengths with coarse spatial resolution. Duan *et al* [16] used artificial neural networks (ANNs) for describing phase-resolved wave forecasts for long-crested waves. The ANN-based wave prediction, which was developed in that study, showed immense potential, as ANNs are most suitable for learning complex patterns, considering nonlinear relationships between the explained and the dependent variables. Furthermore, ANNs are capable of generalizing in noisy environments, which makes them the tool of choice in the presence of incomplete or imprecise data [17].

In our method, we capitalize on both polarimetric sensing and ML methodology by utilizing the latter for inferring the non-trivial association between the reflected light polarization and the sea surface state. This allows for the recovery of the instantaneous water surface slope and subsequently the surface elevation fields. Moreover, benefitting from recent improvements in image processing technology and polarimetric imaging, the system used in the current study is more accessible and affordable than those used in the above-mentioned recent studies. Specifically, the ANN is solving the slope vs. polarimetric data relation for each spatio-temporal point separately and independently, as elaborated in sections 2.2 and 2.4. The methodology and the selection of training sets were driven by the fact the waves of various lengths and steepness generate an ensemble of local slopes, while the polarimetric properties of the reflected light are a function of the local slope regardless of the waves parameters. Here we demonstrate the ability to

reconstruct the slopes ensemble from polarimetric data alone, while using a sufficient training dataset of slopes obtained from simple monochromatic wave (MW) trains. Once trained, the ANN is used as a ML tool, producing near-real-time accurate measurements of complex wave fields in a laboratory setup.

2. Methodology

2.1. Wave field reflected light polarization

Water surface waves are typically described by instantaneous, two-dimensional surface elevation functions in the examined space. Let $\eta(x,y,t)$ and $\nabla\eta(x,y,t)$ be the instantaneous surface elevation and slope, respectively, at point $x,\ y$ in space at time t. Due to wave field's complexity, statistical representations are also used to describe it. Often, a directional waves energy density spectrum is used, achieved by the orthogonal decomposition of the wave field into individual components, each characterized by its frequency, f, or wavenumber vector, k, and by its respective energy and energy propagation direction. Thus, the wave field is described by a superposition of 2D vectors in the $f-\theta$ or $k-\theta$ planes, representing energy density and the directional spread of its propagation [18].

Polarimetric slope sensing (PSS) of water waves exploits polarimetric properties of the skylight scattered from the air–water interface to recover the instantaneous two-dimensional field $\nabla\eta(x,y,t)$ [8]. A camera equipped with linear polarization filters is used to collect water surface polarimetric images, and a physical model is used to describe the $\nabla\eta(x,y,t)$ map inferred from these images [8]. The PSS principle is schematically depicted in figure 1. The light hits the water surface at an incident angle α (measured from the water surface normal) and is reflected toward the image plane. As described by Zappa [8], the incident angle α and the index of refraction n determine the degree of linear polarization, DOLP, defined by:

$$\mathrm{DOLP}(\alpha,n)=\sqrt{\frac{(I_0-I_{90})^2+(2\cdot I_{45}-(I_0+I_{90}))^2}{(I_0+I_{90})^2}} \quad (1)$$

where I_0, I_{45} and I_{90} are the light intensities at $0,\ 45$ and $90°$ linear polarization angles, as detailed in section 2.2. Calculating α from the DOLP is also possible in ideal conditions.

The water surface normal is a negative rotation of the reflected light vector by the angle α, within the plane of reflection. The inclination angle, ϕ, of the plane of reflection is known from the polarization angle $\Phi=90°+\phi$, which can be written as

$$\Phi=\frac{1}{2}\tan^{-1}\left(\frac{(2I_{45}-(I_0+I_{90}))}{(I_0+I_{90})}\right) \quad (2)$$

and completes the specifications of the surface normal [8]. Note that the reflected light vector is specified by the (x,y) coordinates of the point of reflection, obtained with the help of the image geometric calibration process. Therefore, (α,ϕ) and the (x,y) coordinates together specify the orientation of the water surface normal and the associated water surface slope.

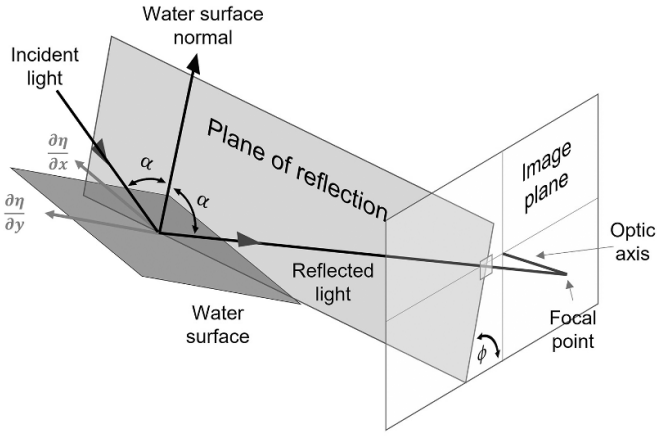

Figure 1. The geometric relationship between the surface normal, incidence angle relative to the water surface (α), polarization orientation (ϕ), and water surface slopes in x and y directions. Reproduced from [8]. © IOP Publishing Ltd. All rights reserved.

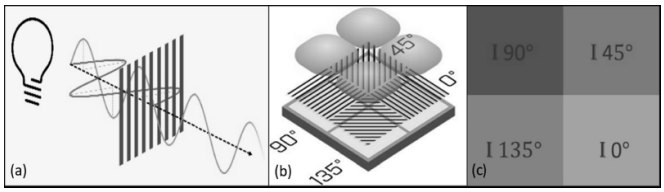

Figure 2. (a) The polarizing filter passes the beam that is aligned to the angle of the slits, and blocks the beam aligned perpendicular to them. (b) Each individual pixel has its own polarizing filter. (c) Zoom in image of the polarimetric image (Reproduced with permission from **Teldyne FLIR**).

In this work, we construct a learnable estimator that receives the light intensities filtered at four linear polarizations in each spatio-temporal image point, as well as the spatial coordinates of that point, while providing the corresponding local water surface slope.

2.2. Setup

The raw data was acquired by a polarimetric camera (Sony IMX250MZR, 2448×2048 pixels, Polar-Mono), equipped with a matrix of linear polarization filters (figure 2(a)) fitted over the camera sensor. The filters are arranged in periodical order, such that each individual pixel has its own polarizing filter. In each 2×2 pixel matrix the filters are oriented at $0°$, $45°$, $90°$ and $135°$, as depicted in figure 2(b).

For each polarimetric image, a region corresponding to the reflection of the light source was selected. The ANN receives as an input a quadruple of pixel intensities corresponding to the four polarimetric pixel light intensities, hereafter denoted as I_0, I_{45}, I_{90}, and I_{135}, respectively. These light intensities are augmented by the $x,\ y$ coordinates corresponding the 2×2 pixels matrix.

The experiments were conducted in the Technion Sea-Air Interactions Research Laboratory wave basin. Flap-type

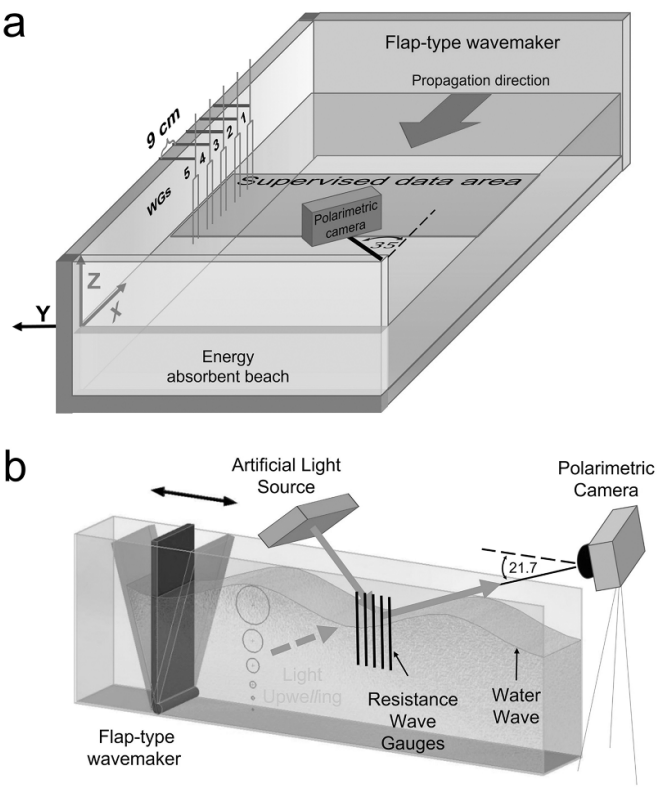

Figure 3. Experiment layouts of supervised data collection in the wave basin of polarized imagery of (a) ArL and (b) AmL reflection on water surface waves generated by wave flap.

mechanical wavemakers[4] (Edinburgh Designs®) were used to generate propagating waves in the form of MW trains and irregular wave fields of a JONSWAP [19] prescribed power density spectral shape, hereafter denoted as SW. The latter served as an approximator of wind-driven waves in the open sea (figure 3(a)). For the SW synthesis, Edinburgh Designs'® wave-generating software[5] was used.

Accurate measurements of the water surface elevation fluctuations were collected by an array of five resistance-type WGs. The WGs array geometry was prescribed by the measured wave field: due to the unidirectionality of the wave trains generated in the wave basin, the five WGs were deployed in-line along the basin x axis (waves propagation direction), assuming wave field uniformity along the y axis. The distance between each WG was set at 9 cm, as depicted in figure 3(a), and the sampling frequency was set at 128 *Hz*.

As the generated waves are characterized by smooth water surface and do not include breaking waves, we can assume surface elevation and slope continuity. The water surface elevation $\eta(x,t)$, and slope $\nabla\eta(x,t)$ in any of the points between the WGs were inferred using spline interpolation of water surface elevation point measurements at the WG locations. Using uniformity along the y axis, the splines were then translated into $\eta(x,y,t)$ and $\nabla\eta(x,y,t)$ 3D maps. As mentioned earlier, the slope maps constituted the target datasets used in the ANN's training. The elevation maps were used as an additional ground truth data for further ANN performance evaluation, as detailed in section 2.7.

Two different light sources were used in this study: an artificial light source and an ambient natural light, hereafter denoted as ArL and AmL, respectively. The ArL source was an in-house made array of nine incandescent lamps fitted with a light diffuser fabric. The WG array was positioned in proximity to the ArL reflection on the water surface (figure 3(b)) to provide an accurate representation of $\eta(x,y,t)$ at the illuminated area. $\eta(x,y,t)$ and $\nabla\eta(x,y,t)$ 3D maps at a given time t were coupled with the corresponding image synchronously captured by the camera equipped with polarization filter. Using the AmL provided illumination of the full field of view of the camera. The data provided by the WGs, recorded at 128 *Hz*, was down-sampled to match the image acquisition rate of each experiment by window averaging sets of data points corresponding to a single frame time span. The camera position was set at a 35° yaw (arbitrarily selected), to the propagation direction of the waves and a $-21.7°$ pitch. A 25 mm focal length lens was used.

2.3. Spatial calibration of the camera field of view

The goal here was to infer the wave field in the real-world coordinate system (RWCS) from polarized light images in the camera's coordinate system (CCS). Thus, the mapping from CCS to RWCS was required. For the calibration, let U and V be the axes of the CCS, with the origin located at the upper-left pixel of the image (figure 4), and let x and y define the RWCS, with its origin set at the lower left corner of the water basin on the mean water level (MWL) as shown in figure 3(b). An affine transformation, $T:\ \{U,V\}\rightarrow\{x,y\}$, is then required to calculate the orientation of the water surface normal relative to the horizontal. This was obtained by traditional geometric calibration using a floating checkerboard on the water surface providing ground control points (figure 4).

Once the calibration was obtained, a matrix was formed containing matching x, y coordinates for every pixel. This enabled transformation of polarimetric data from the camera domain, CCS, to infer the surface slopes in the real-world domain, RWCS. Once the latter was completed, each pixel in the image was assigned into a matrix with the corresponding elevation and slope values.

2.4. Data selection

The polarimetric camera captures the polarized light source reflection from the water surface. The light intensity of each polarized pixel is presented by an integer value in the $0-255$ range, with zero representing a completely dark pixel and 255 representing light saturation. When a pixel is completely dark, it means it is not reflecting any light, whereas when a pixel undergoes light saturation, the light intensity function reaches its maximal value and the information concerning the actual light intensity fluctuations is lost. In the ArL setup, the training

[4] Edinburgh Designs—Wave Generator www.edesign.co.uk/product/ocean-flap-wave-generator/.

[5] Edinburgh Designs—Wave generating software www4.edesign.co.uk/product/wave-generating-software/.

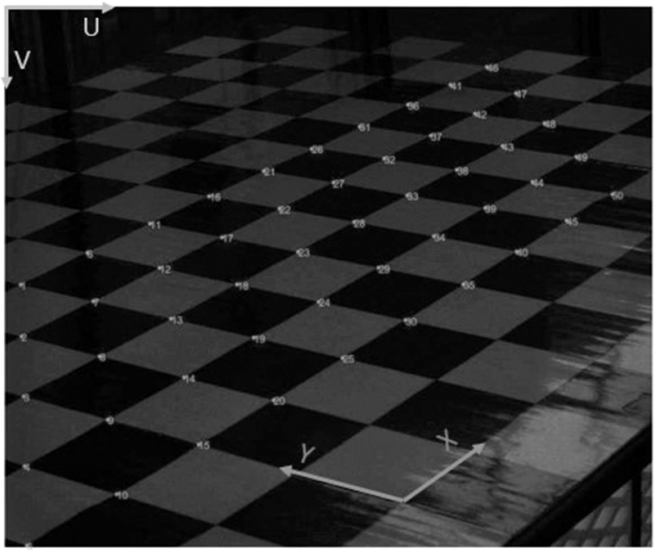

Figure 4. Image of the checkerboard placed on the MWL of the wave basin, RWCS X–Y plane, with the markings of 50 fixed points used for the camera's geometrical calibration.

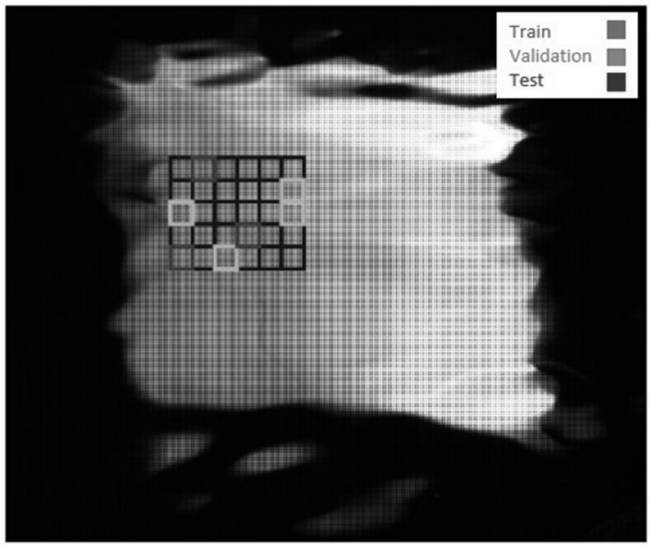

Figure 5. Polarimetric reflection under the ArL, with cell selection and spatial averaging of 40 × 40 pixels for ANN training.

data sets were selected in areas of the image in which the pixels showed no light saturation nor complete darkness.

2.5. Pre-processing

The supervised datasets intended for the ANN training, both inputs and targets, were pre-processed to assure best results. All the measured signals were visually and statistically inspected, and grossly erroneous data were screened out. Next, to reduce noise and neglect small spatial variations, regions of pixels, denoted as *cell s*, were manually delineated for spatial averaging. The selected *cell* area was required to be small enough in comparison with the wavelengths to ensure sufficient spatial resolution in view of the expected water surface slope variations. Here, the *cell* size was set to non-overlapping 40×40 pixels, which correspond to about 4 cm^2 in RWCS.

Once the *cell* size and location were selected, the input and target datasets were averaged over it. The spatial calibration provided the *cell*'s real-world coordinates and enabled us to also spatially average the target wave slopes. These inputs and targets, over consecutive time frames, constituted the available dataset. Thus, the input and output lie in $\mathbb{R}^6$ and $\mathbb{R}^2$ respectively, with $\#Cells\ x\ \#Frames$ input-output pairs.

2.6. ANNconfiguration and training

For estimating $\frac{\partial \eta}{\partial x}, \frac{\partial \eta}{\partial y}$, a multilayer feed-forward fully connected neural network was used. The input to the ANN was the four averaged intensities (spatially averaged over the dimensions of each *cell*) filtered at the different linear polarization angles and the $x,\ y$ center coordinates of each *cell*. The ANN architecture and the hyperparameters were determent experimentally as described below. The network was trained on MW (MW train) data. The training process relied on the backpropagation algorithm and adjusted the weights and biases of the network's neurons by minimizing the mean square error (MSE) loss function for each prediction-target pair i

$$\mathrm{MSE} = \frac{1}{n}\sum_{i=1}^{n}(\pi_i - \overline{\pi_i})^2. \tag{3}$$

Here $\overline{\pi_i}$ denotes the ANN output estimation and π_i the ground truth targets of the water surface slopes provided by the WGs.

To increase generalization, a standard $L2$ regularization term was added to the net objective function:

$$\min_{w \in R} \mathrm{MSE} + \lambda \|w_2\|, \tag{4}$$

where λ is the regularization hyperparameter and w are the network weights.

The MATLAB shallow neural networks toolbox [20] was used to construct and train the networks. The datasets were partitioned into training, validation, and test sets by randomly allocating different *cell*s to each of the three sets (without overlap) as demonstrated in figure 5. The training set was used for the backpropagation process. The validation set was used for estimating the test error and regularizing the network using early stopping if the network overfitted the training data. The test sets were then used for evaluating the trained ANNs performance, as described in detail in section 2.7.

To search for preferred hyperparameters, first a standard random search was performed, within a manually selected range for each hyperparameter. After which an additional finer grid search was conducted around the initially obtained values for fine tuning and validity testing [21]. The search procedure was performed to identify preferred number of hidden layers, number of neurons in each layer and λ $L2$ regularization factor. In addition, an exploratory analysis was performed to identify the preferable activation function and optimization algorithm. The procedure yielded eventually the ANN's architecture and

Table 1. Supervised data sets for ANN training, validation, and test.

Experiment	Lighting conditions	Mechanically generated waves	#Cells	#Frames	Image frame rate [Hz]	Recorded light intensity mean std	ANN architecture	L2 regularization factor (λ)	ANN used for test data reconstruction
MW_{exp1}	*Artificial light source (ArL)*	*Mono-chromatic (MW)*	*30*	*900*	*64*	*40.57*	*10 hidden layers of 42 neurons*	10^{-4}	*Net1*
MW_{exp2}	*Ambient light (AmL)*	*Mono-chromatic (MW)*	*315*	*300*	*16*	*9.31*	*7 hidden layers of 58 neurons*	0	*Net2*
SW_{exp}	*Ambient light (AmL)*	*JONSWAP spectral shape (SW)*	*495*	*1800*	*16*	*9.58*	*7 hidden layers of 58 neurons*	0	*Net2*

hyperparameters corresponding to the highest Pearson correlation coefficient, R, between the ground truth slopes and the network estimates. As the MSE and R cover two different aspects of the net's reconstruction capabilities, training on the MSE and validating on the R optimizes the net's performance on both aspects [22]. This experiment was conducted under ArL and *AmL* conditions to account for the effect of light and different configurations. These are detailed in table 1.

Once trained, the ANN became a parametric description of the approximated connections between the optical water surface light reflection properties as sensed by polarimetric imaging and the water surface waves properties.

2.7. Trained ANN evaluation and post processing

The ANN's wave slope reconstruction capabilities were evaluated in several different configurations. In the first experiment, we tested the slope estimation on the MW train. The test samples were taken from the same set of data used for training and validation, but naturally were not included in the training process (see figure 5). This evaluation was repeated for both artificial and ambient lighting conditions.

While the training was held on MW, it was expected that light polarization would not be affected by the irregularity of the slope variations in wave fields of finite spectral width. Thus, the same trained network should be able to infer irregular wave fields as well. To challenge this hypothesis, the trained network capabilities were next evaluated on additional polarimetric images taken from supervised data sets of SW.

The third set of evaluations were done in terms of reconstructing the energy density spectrum of the SW. The ANNs provided the surface slopes, however, to estimate the energy density spectrum, we needed to obtain the elevation maps $\eta(x,y,t)$. Therefore, the estimated 2D surface slopes $\nabla\eta(x,y,t)$ were integrated numerically, and a single WG point measurement served as the integration constant in each time step, t,

$$\eta(x,y,t) = \iint \nabla\eta(x,y,t)\,\partial x\partial y + \eta_{wg}(x_0,y_0,t). \qquad (5)$$

To obtain a unique solution of equation (5) a regularized least-squares surface reconstruction from gradient fields algorithm was implemented, which solves the Sylvester equations with additional form of regularization [23, 24]. Once the $\eta(x,y,t)$ maps were obtained, they were processed to obtain the energy density spectrum and compared with the spectrum obtained by the WG measurements.

Data availability covering a much larger spatial region under the *AmL* conditions led to higher wavenumber resolution in the spectral domain. This made producing the directional spectrum possible. No direct comparison to ground truth was possible in this case as no other directional measurement technique was available for these experiments. Instead, the quality of the reconstructed waves directional energy density spectrum was validated by examining known wave field parameters set by the mechanical wavemaker operation, the camera viewing angle, and the measurements of the WGs.

3. Results and discussion

In our study, three laboratory experiments were conducted for supervised data collection, as detailed in table 1. In all the training of the ANN, the optimization algorithm found to yield the best performance was the gradient descent with momentum and adaptive learning rate. The activation function that returned the lowest MSE was the hyperbolic tangent, tanh.

3.1. Monochromatic propagating wave train under artificial light source experiment—MW_{exp1}

In MW_{exp1}, the simple case of an MW with the controlled *ArL* reflection measurements was examined. A propagating MW train of 1 Hz frequency and 2.1 cm amplitude was generated. This resulted in a 1.55 m wavelength, with $kh = 2.837$ and steepness of $ak = 0.085$. 900 image frames were collected at a 64 Hz framerate. The 30 selected *cell*s over the 900 frames (table 1) yielded a dataset of 2.7×10^4 samples. Next, the dataset was split into training, validation, and test sets, as detailed in section 2.6 and demonstrated in figure 5.

The exploratory analysis for preferred network hyperparameters architecture yielded a net architecture of 10 hidden layers with 42 neurons in each and an $L2$ regularization factor of $\lambda = 10^{-4}$ (see table 1). The ANN training process evaluation on the preferred architecture can be seen in the scatter plots

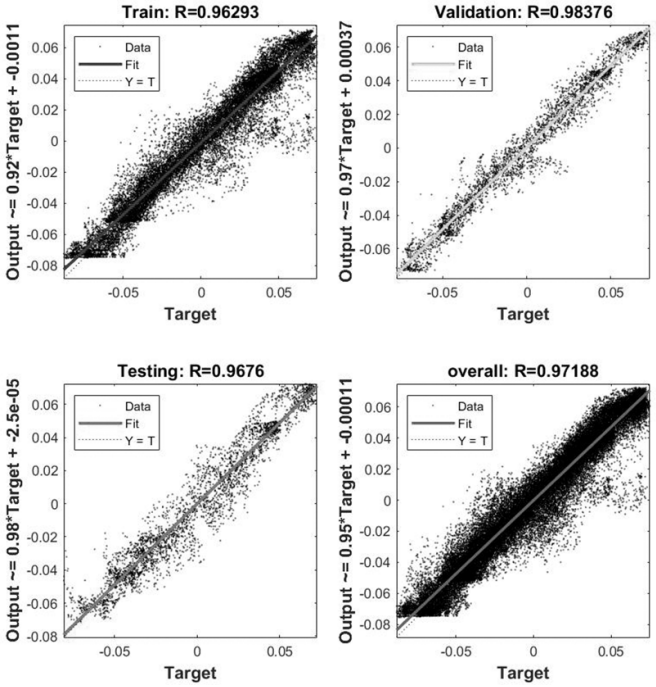

Figure 6. MW_{exp1} linear regression R of Net1 outputs vs targets in training, validation, test sets, and overall.

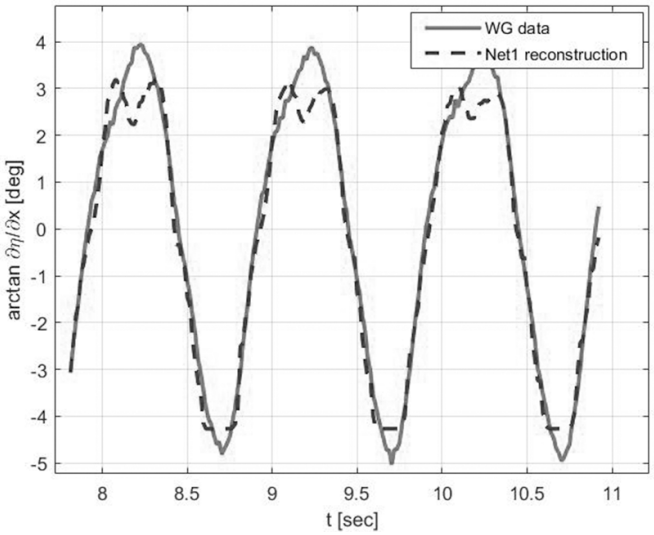

Figure 7. MW_{exp1} $\tan^{-1}(\partial\eta/\partial x)$ of representative test set time series, ANN output vs. targets.

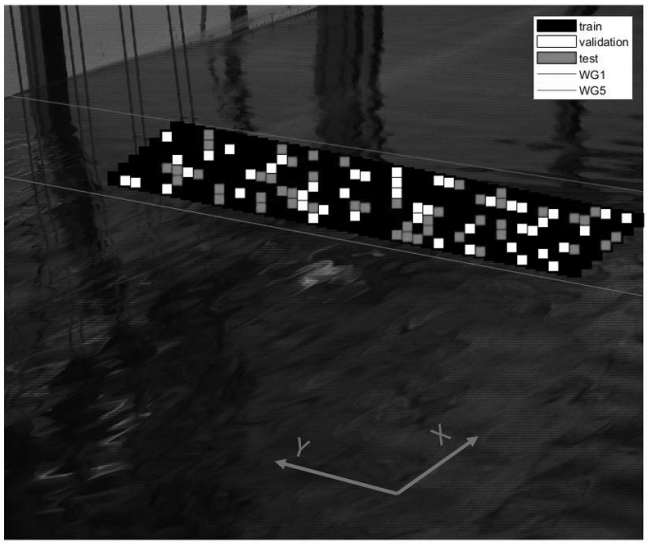

Figure 8. MW_{exp2} image of AmL polarimetric reflection, with a *cell* selection and spatial averaging of 40×40 pixels for ANN training. The area between the lines is the supervised data area covered by the WGs' measurements.

(figure 6) of the network's output vs. the targets on the training, validation, and test sets and overall. $R = 0.9676$ was reached.

The results of the slope reconstruction by the trained MW_{exp1} net of *cell* test data vs. the WGs' measurements is shown in figure 7. The WGs' measurements and the network's estimates are marked in continuous and broken lines, respectively. The MW_{exp1} net, denoted as *Net*1 (see table 1), captured the overall wave period well, while the reconstruction accuracy of the instantaneous slope fluctuations varied. Both the positive and negative maxima values of the slope variations were slightly underestimated. However, as the extreme values of the slope correspond the surface elevation instances close to the MWL, such reconstruction results can be considered largely satisfactory.

3.2. Monochromatic propagating wave train under ambient light experiment—MW_{exp2}

The MW_{exp2} was conducted to further evaluate the robustness of the ML-aided reconstruction method by increasing the complexity of the polarimetric data. Thus, a setup similar to the MW_{exp1} experiment was implemented, except for removing the *ArL* source and producing the polarimetric reflection measurements under *AmL* (Table 1). Examining the variations of the recorded light intensity revealed lower signal standard deviation, *std*. This indicated the need to increase the light intensity variations range captured in each pixel. To this end, longer exposure time was selected, and the image collection frame rate was reduced to 16 Hz (table 1). Alleviating the constraint of the small area reflecting the *ArL*, all the data in the WGs measurements, under the assumption of wave uniformity along the *Y* axis, was considered as the training dataset. Hence, a much larger training dataset was constructed, constituting 315 fixed *cell*s over 300 frames (see table 1), yielding an overall data set of 9.45×10^4 samples. Figure 8 presents the selected *cell* split for training, validation, and test, covering the maximal available spatial information bounded by the area covered by the WGs measurements. The black squares represent the train set, the white squares represent the validation set, and the gray squares represent the test set.

Once again, an exploratory analysis was performed to find the best network's hyperparameters and architecture. The following parameters were found to provide the best results: a net architecture of 7 hidden layers of 42 neurons each and no *L*2 regularization factor, meaning $\lambda = 0$. The trained MW_{exp2}

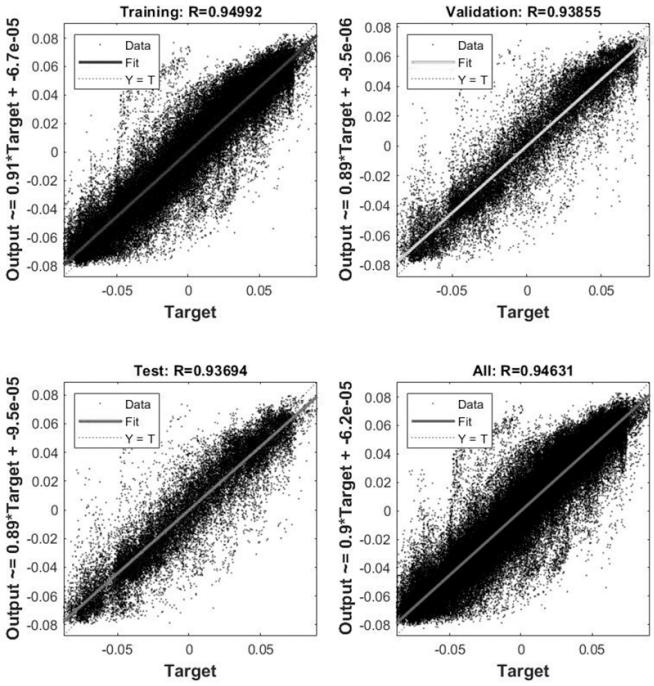

Figure 9. $\mathrm{MW_{exp2}}$ linear regression R of Net2 outputs vs targets in training, validation, test sets, and overall.

net, denoted as the *Net*2 (see table 1) evaluation, reached $R = 0.93694$, as depicted in figure 9.

Figure 10 presents the $\mathrm{MW_{exp2}}$ *Net*2, in AmL conditions. The reconstruction capabilities of *cell*s are not included in the training process vs. the WGs' measurements. The WGs' measurements and the network's estimates are marked in continuous and broken lines, respectively. The results suggest a less accurate performance in the net's capability to reconstruct $\nabla\eta\,(x,y,t)$ when compared to the results of the set using *ArL* in $\mathrm{MW_{exp1}}$. However, despite the obvious reconstruction accuracy reduction, the net still captures the overall wave period well and produces comparable underestimation of the slope variations maxima, in a less controlled experiment and over a much larger reconstruction area.

3.3. JONSWAP spectrum wave field under ambient light experiment—SW_{exp}

For SW reconstruction, the *Net*2 network that was trained on $\mathrm{MW_{exp2}}$ under the *AmL* was used without further modification (table 1). The test set in SW_{exp} was obtained by creating a supervised set of an irregular wave field corresponding to the JONSWAP spectral shape, formulated by

$$S = \alpha_{\mathrm{p}} \cdot g^2 \cdot \omega^{-5} \cdot \exp\left[-\frac{5}{4}\cdot\left(\frac{\omega_{\mathrm{p}}}{\omega}\right)^4\right] \cdot \gamma^{\exp\left(-\frac{(\omega-\omega_{\mathrm{p}})^2}{2\sigma^2\cdot\omega_{\mathrm{p}}^2}\right)}. \quad (6)$$

The spectral parameters were the peak time period $T_{\mathrm{p}} = 0.66$ sec, peakiness coefficient $\gamma = 3.3$, and central frequency $f_{\mathrm{P}} = 1.5$ Hz, with frequency components of significant energy in the range between 1.2 Hz and 2 Hz, as presented in figure 13. This resulted in significant wave height $H_{\mathrm{s}} = 3$ cm, calculated by

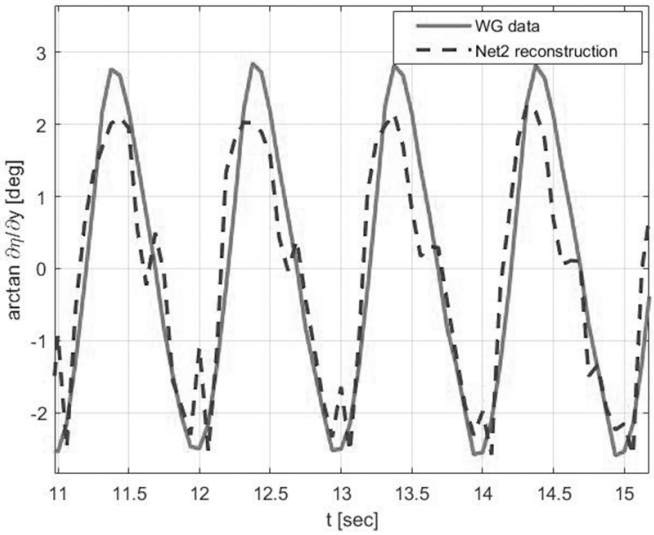

Figure 10. $\mathrm{MW_{exp2}}$ $\tan^{-1}(\partial\eta/\partial y)$ representative test set time series, ANN output vs. targets.

Figure 11. $\mathrm{SW_{exp}}$ image of AmL polarimetric reflection and the selected *cell*s. The area between the lines is the supervised data area covered by the WG measurements.

$$H_{\mathrm{s}} = 4\cdot\left(\int_0^\infty S(f)\,\partial f\right)^{0.5}. \quad (7)$$

495 fixed *cells* over 1800 frames were selected (table 1), yielding a test dataset of 8.91×10^5 samples. The *cells* selected for reconstruction by the trained ANN, using the maximum available spatial information bounded by the area measured by the WGs, are marked between the two grey lines in figure 11.

The net outputs of $\nabla\eta\,(x,y,t)$ were then integrated numerically, solving equation (5) [23, 24], to obtain the $\eta\,(x,y,t)$ maps in each time frame. The integration coefficient was provided by WG1 (figure 3(b)) measurements, sampled at 16 Hz identical to the camera frame rate. This resulted in

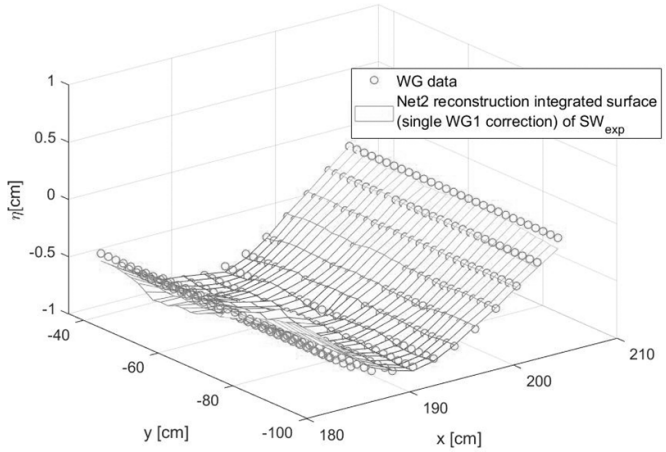

Figure 12. SW_{exp} region of interest, representative example of the instantaneous $\eta(x,y)$, wave gauge measurements vs *Net2* reconstruction.

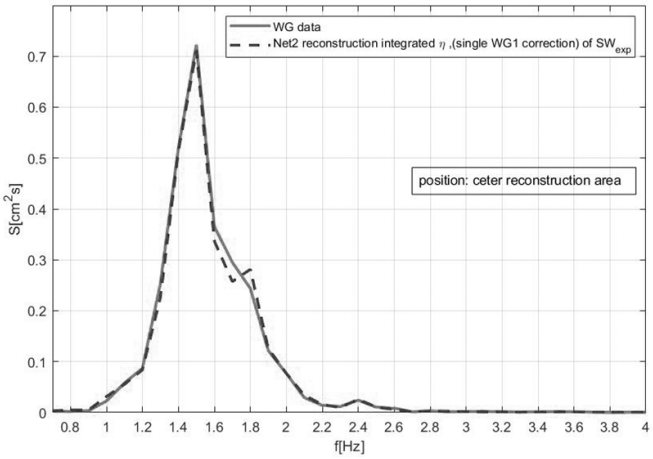

Figure 13. SW_{exp} energy density spectrum of a point at the center of reconstructed area, wave gauge measurement vs reconstruction.

a reconstructed $\eta(x,y,t)$ maps of about 2×2 cm^2 spatial resolution sampled at 16 Hz. A representative example of one frame reconstructed $\eta(x,y,t)$ is shown in figure 12. To mitigate the effects of the observed higher noise-to-signal ratio of the net's output, the reconstructed slopes were spatially averaged in 6×6 *cells*, with 50% and 83% overlap in the x and y axes, respectively, and integrated in the same procedure. This resulted in reconstructed $\eta(x,y,t)$ maps of about 12×12 cm^2 spatial resolution sampled at 16 Hz.

The acquired averaged $\eta(x,y,t)$ maps were then further processed to examine the quality of reconstruction in terms of the waves energy density spectrum and the energy propagation direction and spread. A comparison between the reconstructed energy density spectrum and the ground truth spectrum calculated from the surface elevation fluctuations obtained by WGs is shown in figure 13. The reconstructed spectrum shape compares favorably with the ground truth. The peak energy, the long waves side of the spectrum, and the second harmonic (located at 2.4 *Hz*) match almost perfectly, whereas the spectrum high frequency side reconstruction is somewhat less accurate.

After validating the trained ANN ability to faithfully reconstruct the slopes and the waves energy density spectrum at selected locations, the ANN performance in reconstructing the wave field over the entire image was examined next. Solving equation (5) [23, 24], the net outputs were similarly integrated to obtain $\eta(x,y,t)$ maps, and the directional energy density spectra of those maps were produced. The resulting spectrum, averaged over the full-time span, is presented in figure 14. Within the camera-covered area, the spectral wavenumber resolution is $dk_x = 0.095$ cm^{-1} and $dk_y = 0.101$ cm^{-1} in the x and y directions, respectively. Energy peak is situated at 1.5 *Hz* and the wavenumber $|k|$ ranges between 0.1386 cm^{-1} and 0.2773 cm^{-1}, within the confidence interval, as estimated from the linear theory calculations: 1.5 Hz dominant frequency and $k = 0.0905$ cm^{-1}. The energy propagation direction is noted to be in the range between 28° and 64.8° (the range bounds set by the dk), again in correspondence with

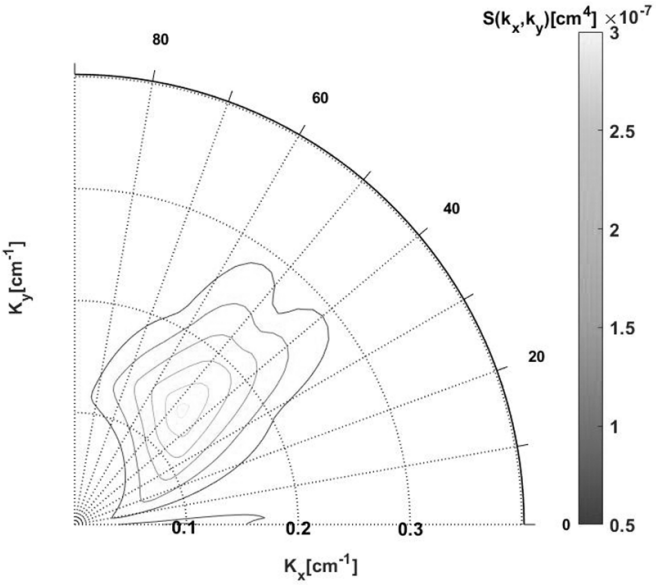

Figure 14. SW_{exp} 2D directional energy density spectrum of whole image area reconstruction.

the expected 35° main direction of propagation relative to the camera point of view. The wavenumber resolution, limited by the current experimental setup in the small wave basin, does not allow the exact evaluation of the reconstruction performance in terms of the energy propagation directional spread. However, the energy propagation direction spread is narrow, as expected for the examined mechanically generated unidirectional wave field. The energy density and the directional spectra validate the developed approach and thus render it as suitable for wave energy density distribution reconstruction in laboratory conditions under AmL.

Finally, to quantitively evaluate the trained nets' overall performance, the root mean square (RMS) of the entire test sets were reconstructed and the target-slope variations were calculated for the above-mentioned three experimental conditions (table 1). In addition, these results were compared with

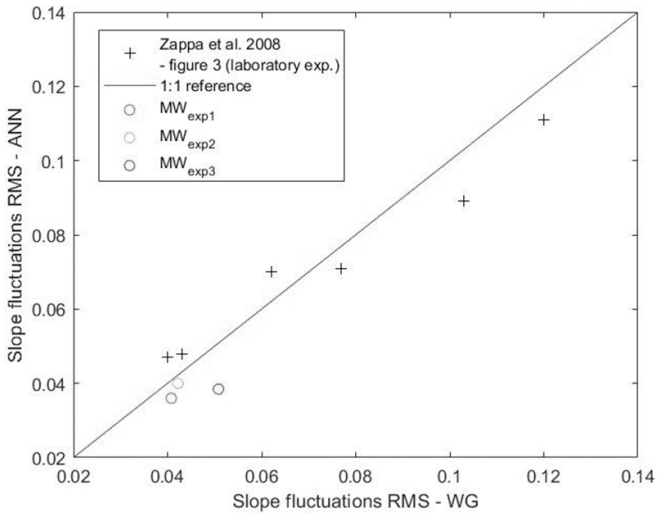

Figure 15. Slope variation RMS, trained net outputs vs targets for the test sets in all experiments for the entire spectrum of wavelengths, compared with Zappa *et al* [8] reconstruction of only the shortest wavelengths.

the laboratory results presented in Zappa *et al* [8]. These are reported in figure 15. Zappa *et al* reported $R = 0.98$ for only very short wavelengths of about 5 Hz. In the results presented here, $R = 0.991$ was obtained for a smaller slope RMS values range, while the major advance offered by the new methodology is reconstructing the slopes of all wavelengths, resolving the full spectrum of wavelengths.

4. Conclusions

The new methodology presented here incorporates ML tools to solve the water surface slope to the reflected light polarization relationship, effectively implementing the PSS concept [8] with the aid of ANNs. We aimed at demonstrating the ability of the new methodology to produce spatio-temporal measurements of water waves in a laboratory environment under both artificial and ambient lighting conditions. We achieved two-dimensional waves slope field reconstruction by remote sensing of polarimetric imaging and ANN training, without enforcing simplifying assumptions on reflected light polarization or water turbidity, while resolving the full spectrum of wave lengths. While resulting in a finite accuracy reconstruction of waves slope variations at single point measurements, the ANN reconstruction products were shown to produce accurate estimations of both the one-dimensional energy density spectrum and the directional energy density spectrum in the $k - \theta$ domain.

The current methodology utilizes the understanding of light reflection geometry change at different locations in the measured wave field, an effect neglected in Zappa *et al* [8] that aimed to reconstruct only the very short waves of the spectrum. Here we incorporate the (x, y) coordinates in the set of ANN input parameters to achieve the demonstrated quality of performance, reconstructing the surface elevation fluctuations' of spectral components of all lengths with significant accuracy as depicted in figure 15, and not only the shortest waves of the spectrum, as demonstrated by spectral shapes comparison and quantified by reconstructed slope fluctuations' RMS.

Examining the reconstruction capabilities of *Net*1 (figure 7) and of *Net*2 (figure 10) a systematic errors in inner period phase perturbation in the maximum and minimum slope values can be observed. Nevertheless, resulting in satisfactory reconstruction of the instantaneous surface elevations. The source and mechanism responsible for the observed systematic error are yet to be determined and are beyond of the scope of the current feasibility study.

The results and open questions provide a strong incentive for further research to further mature the methodology with additional supervised datasets and increased complexity of the ML tools to improve its robustness. The current methodology is based on learning the local slope-polarimetric data relation, hence a viable option would be the use of convolutional neural networks to incorporate neighbors' data, such networks will receive as an input and target a finite size spatial area or the full image, learning the spatial variations. Moreover, a combined spatio-temporal convolutional neural network can be considered, by inputting a set of consecutive images. Furthermore, to enhance the ANN reconstruction capabilities in follow-up studies, we propose the use of one of the existing remote sensing spatial techniques to measure the ground truth for the ANN. targets, which will significantly increase the quality, variety, and spatial availability of data for training. The latter modifications of the system will aid in progressing towards the goal of developing the capacity to accurately reconstruct the instantaneous phase variations. Which in turn will facilitate the obtaining the wave field spectral components celerity vectors directly by near-real-time monitoring.

The success of an artificial network trained on a simplistic, MW train to reconstruct an irregular JONSWAP-prescribed power density spectral shape field, set the path for upscaling from a laboratory setup tool to an open sea application for research, monitoring, and the short-time forecast of waves.

Data availability statement

The data that support the findings of this study are available upon reasonable request from the authors.

Acknowledgments

The authors acknowledge the financial support provided by the Israeli Ministry of Energy Grant No. 1016825; This project was funded in part as well by the Israeli Ministry of Environmental Protection, Grant No. 162-71. Noam Ginio is grateful for the research scholarships provided by the Israeli Port Company (IPC).

ORCID iD

Dan Liberzon https://orcid.org/0000-0003-4061-8203

References

[1] Harald E 2005 Theory, instruments and methods of analysis *Measuring and Analysing the Directional Spectra of Ocean Waves* (Luxembourg: Office for Official Publications of the European Communities) pp 3–14

[2] Toffoli A, Proment D, Salman H, Monbaliu J, Frascoli F, Dafilis M, Stramignoni E, Forza R, Manfrin M and Onorato M 2017 Wind generated rogue waves in an annular wave flume *Phys. Rev. Lett.* **118** 144503

[3] Hashimoto N 1997 Analysis of the directional wave spectrum from field data *Adv. Coast. Ocean Eng.* **3** 103–44

[4] Donelan M A, Drennan W M and Magnusson A K 1996 Nonstationary analysis of the directional properties of propagating waves *J. Phys. Oceanogr.* **26** 1901–14

[5] Bourdier S, Dampney K, Lopez H F G and Richon J-B 2014 Non-intrusive wave field measurement *MARINET Report*

[6] Sun J, Burns S P, Vandemark D, Donelan M A, Mahrt L, Crawford T L, Herbers T H C, Crescenti G H and French J R 2005 Measurement of directional wave spectra using aircraft laser altimeters *J. Atmos. Ocean. Technol.* **22** 869–85

[7] Li H, Avila M and Duo X 2021 A single-camera synthetic Schlieren method for the measurement of free liquid surfaces *Exp. Fluids* **62** 1–15

[8] Zappa C J, Banner M L, Schultz H, Corrada-Emmanuel A, Wolff L B and Yalcin J 2008 Retrieval of short ocean wave slope using polarimetric imaging *Meas. Sci. Technol.* **19** 055503

[9] Smith G S 2007 The polarization of skylight: an example from nature *Am. J. Phys.* **75** 25–35

[10] Baxter B, Hooper B A, Williams J Z and Dugan J P 2009 Polarimetric remote sensing of ocean waves *OCEANS 2009* (IEEE) pp 1–5

[11] Zhang R H *et al* 2020 A review of progress in coupled ocean-atmosphere model developments for ENSO studies in China *J. Oceanol. Limnol.* **38** 930–61

[12] Salin B M and Salin M B 2015 Combined method for measuring 3D wave spectra. I. algorithms to transform the optical-brightness field into the wave-height distribution *Radiophys. Quantum Electron.* **58** 114–23

[13] Cannata A, Cannavò F, Moschella S, Giuseppe Di G, Nardone G, Orasi A, Picone M, Ferla M and Gresta S 2020 Unravelling the relationship between microseisms and spatial distribution of sea wave height by statistical and machine learning approaches *Remote Sens.* **12** 761

[14] Shao W, Ding Y, Li J, Gou S, Nunziata F, Yuan X and Zhao L 2019 Wave retrieval under typhoon conditions using a machine learning method applied to Gaofen-3 SAR imagery *Can. J. Remote Sens.* **45** 723–32

[15] James S C, Zhang Y and O'Donncha F 2018 A machine learning framework to forecast wave conditions *Coast. Eng.* **137** 1–10

[16] Duan W, Ma X, Huang L, Liu Y and Duan S 2020 Phase-resolved wave prediction model for long-crest waves based on machine learning *Comput. Methods Appl. Mech. Eng.* **372** 113350

[17] Mas J F and Flores J J 2008 The application of artificial neural networks to the analysis of remotely sensed data *Int. J. Remote Sens.* **29** 617–63

[18] Dean R G and Dalrymple R A 1984 *Water Wave Mechanics for Engineers and Scientists* (Singapore: World Scientific Publishing) (https://doi.org/10.1142/1232)

[19] Hasselmann K 1973 Measurements of wind-wave growth and swell decay during the joint north sea wave project (JONSWAP) *Ergnzungsheft Zur Deutschen Hydrographischen Zeitschrift Reihe* A **46** 95

[20] Beale M H, Hagan M T and Demuth H B 2016 Neural network toolbox ^{TM} reference 255

[21] Bengio Y, Goodfellow I and Courville A 2017 *Deep Learning* vol 1 (Cambridge: MIT press)

[22] Caballero L, Jojoa M and Percybrooks W S 2020 Optimized neural networks in industrial data analysis *SN Appl. Sci.* **2** 1–8

[23] Harker M and O'leary P 2022 Surface reconstruction from gradient fields: grad2Surf version 1.0 *MATLAB Central File Exchange* (available at: www.mathworks.com/matlabcentral/fileexchange/43149-surface-reconstruction-from-gradient-fields-grad2surf-version-1-0) (Accessed 12 December 2022)

[24] Harker M and O'leary P 2015 Regularized reconstruction of a surface from its measured gradient field *J. Math. Imaging Vis.* **51** 46–70